




Key physical descriptors for predicting interfacial thermal resistance by machine learning

Cite as: J. Appl. Phys. **137**, 245302 (2025); doi: [10.1063/5.0274575](https://doi.org/10.1063/5.0274575)

Submitted: 7 April 2025 · Accepted: 9 June 2025 ·

Published Online: 25 June 2025



Xiaohan Song,  Weidong Zheng,  Haoqiang Ai,  Hao Zhou,  Liyin Feng,  Zheng Cui, 
and Ruiqiang Guo  ^{a)}

AFFILIATIONS

Thermal Science Research Center, Shandong Institute of Advanced Technology, Jinan, Shandong 250103, China

^{a)}Author to whom correspondence should be addressed: ruiqiang.guo@iat.cn

ABSTRACT

Interfacial thermal resistance (ITR) plays a crucial role in the thermal management of micro-nano devices. Compared with traditional approaches, machine learning is a cost-effective, accurate, and efficient method for predicting material properties, but its limited interpretability hinders the exploration of underlying mechanisms. In this study, we have constructed machine learning models that can effectively predict ITR by comparing six algorithms, with the random forest (RF) model achieving the highest accuracy. Through feature engineering, 39 descriptors have been narrowed down to 7 descriptors while maintaining accuracy, among which 5 descriptors are all strongly related to the bonding strength and, thus, the vibrational properties of the two materials consisting of the interface. In particular, we have defined new descriptors corresponding to the matching degree of the sound velocity and applied it to obtain an improved RF model. We further employed this improved RF model to explore materials with a low ITR when in contact with Si, providing guidance for the search of chip heat dissipation materials. The key physical descriptors agree well with the physical picture of phonon transport across interfaces and enhance the interpretability of the machine learning models, which can accelerate the design and optimization of thermal interfaces in relevant applications.

© 2025 Author(s). All article content, except where otherwise noted, is licensed under a Creative Commons Attribution (CC BY) license (<https://creativecommons.org/licenses/by/4.0/>). <https://doi.org/10.1063/5.0274575>

I. INTRODUCTION

With the continuously increasing power density and miniaturization of electronic devices, thermal management in electronic packaging has garnered widespread attention in recent years.^{1–5} Interfacial thermal resistance (ITR) is a critical factor affecting the heat dissipation of micro-nano devices.^{3,6–9} Low ITR facilitates more efficient heat transfer from high-temperature regions to heat sinks and, thus, helps mitigate the failures and performance degradation of devices caused by overheating. Therefore, it is vital to accurately determine the ITR and design material interfaces with targeted ITR for the thermal management of electronic devices.

The realm of predicting ITR has been explored through traditional theoretical models such as the Acoustic Mismatch Model (AMM), Diffuse Mismatch Model (DMM), and Scattering-Mediated Acoustic Mismatch Model (SMAMM).^{10–12} These models can provide valuable insights into the underlying mechanisms of interfacial phonon transport and have guided efforts to mitigate ITR.^{13,14} However, the AMM and DMM models are generally used as a qualitative tool due to their limited precision and

reliability. Large discrepancies between their prediction and experimental/computational results have been commonly observed in previous studies.^{15–17} In addition to these models, the ITR can be calculated using several traditional approaches, including molecular dynamics (MD), non-equilibrium Green's function (NEGF) approach, and phonon Boltzmann transport equation (BTE).^{3,6,18–21} These approaches could provide some insights into phonon transport across interfaces in details, such as the temperature distribution and phonon transmission.^{22–26} However, the significant computational expense and the considerable reliance on interatomic potentials largely limit their applicability for the design of ITR. Considering the limitations of these traditional tools, new methods for predicting ITR are highly desired.

In recent years, machine learning has emerged as a powerful tool in solving challenging thermal issues.^{27–35} Machine learning models can achieve fast and accurate prediction of materials properties, making it possible to efficiently search for target materials and properties. For example, Yang *et al.* employed a neural network model to predict ITR between graphene and h-BN.³⁶

28 June 2025 08:06:18

Guo *et al.* realized rapid and accurate prediction of heat transfer and adsorption at microscopic solid–liquid interface by combining MD and convolutional neural networks.³⁷ Wu *et al.* employed three machine learning algorithms to predict ITR and achieve a high prediction performance of 96%, through incorporating 35 descriptors based on physical, chemical, and material properties of the interface conditions.³⁸ Liu *et al.* successfully predicted the thermal conductivity of polymer composites with a single filler and oriented one-dimensional fillers.^{39,40} In addition to the prediction of the thermal properties of materials, machine learning has also been widely applied to the prediction of mechanical, electrical, electrochemical, and other material properties.^{41–47} The utilization of machine learning methods for ITR can greatly enhance the accuracy and efficiency of predictions, thereby significantly reducing experimental costs and time. However, the limited interpretability of machine learning models hinders the understanding of mechanisms underlying interfacial heat conduction. The investigation of key physical descriptors for ITR is highly desired and would greatly improve the interpretability of machine learning models.

In this article, the machine learning approach has been successfully employed to construct models for ITR of materials, and the key physical descriptors of ITR were identified. It is found that all six machine learning regression algorithms, namely, Support Vector Machines (SVM), Random Forest (RF), Decision Tree (DT), Gradient Boosting Decision Tree (GBDT), Gaussian Process (GP), and Neural Network (NN) could effectively describe ITR with accuracies R^2 above 0.93, among which RF exhibited the highest accuracy. Also, feature engineering is conducted to eliminate unnecessary descriptors, reducing the number of descriptors from 39 to 7 while maintaining similarly high accuracy. Five of the selected descriptors describe the physical properties of the film and the substrate, all strongly depending on the bonding strength and, thus, vibrational properties of the two materials at the interface. Furthermore, ITR exhibits a negative correlation with the ratio of the square root of bulk modulus (or shear modulus) over the density of film and substrate materials, i.e., the ratio of the sound velocity, which enhances the physical interpretability of predicted results by machine learning. The RF model retrained with the new descriptors including the ratio of the square root of bulk modulus (or shear modulus) over density achieves higher accuracy than the previous RF models. Finally, a prediction dataset was constructed based on the RF model to explore materials with a low ITR when contacting Si.

II. METHODS

A. Data and descriptors

Figure 1(a) shows a schematic interface consisting of film and substrate materials, across which a sharp temperature drop occurs due to a large ITR. In this study, we use experimental values of ITR from the literature to construct machine learning models. Specifically, the original dataset in this study comprises 663 experimental data, consisting of 247 interfaces and 32 materials, which is collected from the dataset organized by Xu *et al.*^{38,48,49} To ensure data consistency and reliability, the dataset excludes the metal/metal interfaces and only includes the metal/non-metal and non-metal/non-metal interfaces, considering that the heat conduction

mechanism in the former largely differs from the latter. Also, two-dimensional materials, materials with uncertain ratio and specially treated interfaces are excluded. The uncertainty of the measured ITR depends on the measurement techniques and sample quality, especially the interface quality. For some interfaces, there exists an interlayer between the film and the substrate, which can be an adhesion layer, a naturally or thermally formed oxidation layer, or an ultrathin film or mixed region formed by surface plasma treatment.

The collected data from literature studies include ITR, chemical formula of material systems (films, substrates, and interlayer materials) at the interface, measurement temperature, film thicknesses, relevant material preparation methods, ITR measurement techniques, and other details. The physical and chemical properties of the materials at the interface were sourced from databases such as the thermoplastic composites research center (TPRC) data series, AtomWork-Adv by the National Institute for Materials Science (NIMS).

The construction of initial machine learning models considered 39 descriptors, among which 35 descriptors were previously suggested by Xu *et al.*^{38,48} In particular, considering the strong influence of the elastic modulus on ITR, the bulk modulus (bm) and shear modulus (sm) of both the thin film and the substrate were further incorporated into the property descriptor set in the present study. The corresponding data were collected from the Materials Project database (<https://next-gen.materialsproject.org/>).^{50,51} As shown in Table I, these descriptors were categorized into three sets (property descriptors, compound descriptors, and process descriptors), similar to the previous treatment.^{38,48} Property descriptors include the physical thermal properties of the materials at the interface, such as temperature (T), specific heat capacity (heatcap), melting point (melt), density, unit cell volume (unit), bulk modulus (bm), and shear modulus (sm). Compound descriptors indicate the chemical properties of the interfaces, such as atomic ratio (R), atomic coordinate (AC), mass, binding energy (Eb), electronegativity (ENc and ENa), and ionic potential (IPc and IPa) for cation and anion. The atomic ratio was expressed as R1 and R2, representing the number of atoms of the first and second elements in the compound in the formula, for example, R1 and R2 of SiO₂ are 1 and 2. The atomic coordinates were represented as (AC_{ix}, AC_{iy}), where *i* is the order of the elements of the compound, and *x* and *y* represent the group and period of the element in the periodic table, for example, the atomic coordinates of (AC_{1x}, AC_{1y}) and (AC_{2x}, AC_{2y}) for SiO₂ are (14, 3) and (16, 2). Process descriptors consist of properties that can be adjusted during the experiment, such as the film thickness (fthick) and the interlayer. Here, interlayer denotes whether there is an interlayer between the materials at the interface, with a value of 1 indicating its presence and 0 indicating its absence. Here, the descriptors of the thin film and the substrate are denoted as “f” and “s”, respectively. Notably, the dataset lacks a descriptor for interface roughness, mainly due to the absence of corresponding data in the literature. Given the critical role of interface roughness in determining ITR, its absence may reduce the accuracy of machine learning models for predicting ITR.

B. Machine learning models

In order to construct accurate machine learning models, six machine learning algorithms were attempted, including SVM, RF,

28 June 2025 08:06:18

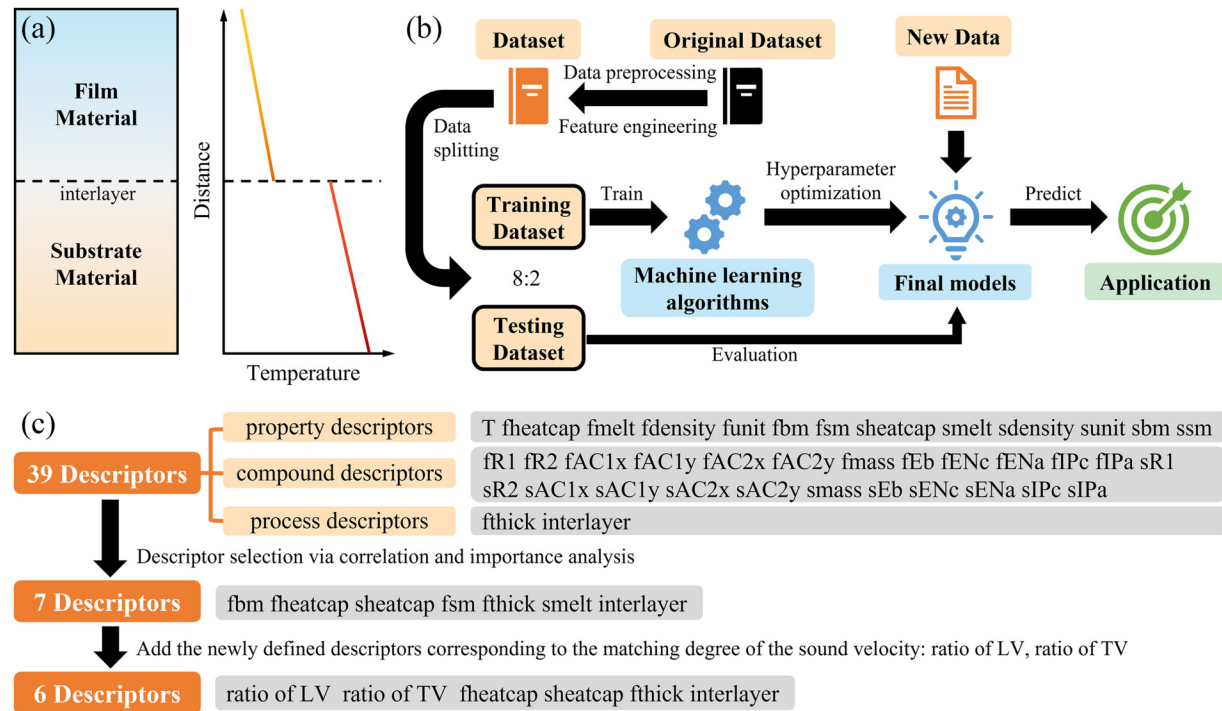


FIG. 1. (a) Schematic diagram and temperature profile of the interface consisting of the substrate material and the film material, with an interlayer at the interface. (b) Schematic diagram of the machine learning training process. (c) Flowchart of the feature engineering process.

DT, GBDT, GP, and NN. These algorithms were implemented using the scikit-learn package.⁵² The machine learning workflow is illustrated in Fig. 1(b). Starting from the original dataset, data preprocessing and feature engineering were performed to prepare the working dataset. This dataset was then randomly split into training and testing sets, which comprise 80% and 20% of the total data, respectively. The training set was used to train the machine learning models, and the testing set was employed for model evaluation after hyperparameter optimization. Once the final model is established, it can be applied to predict the properties of new data for practical applications.

In the data preprocessing stage, feature normalization was applied specifically for the training of the NN model. It is worth noting that the dataset used in this study comprises 663 experimental data points. Although this size is sufficient for initial model development and descriptor analysis, it is still relatively limited and may constrain the generalizability of the trained models as well as the statistical robustness of the conclusions. To ensure robustness and reduce the influence of data splitting, we performed five random splits for each model and averaged the model evaluation results. For each split, a fivefold cross-validation was employed on the training set to address overfitting during model training. Grid search optimization was performed to fine-tune the hyperparameters of each model. The hyperparameter configurations yielding the best cross-validation performance were selected as the optimal values. For each algorithm, a representative model was selected from five dataset splits, with the

detailed hyperparameters listed in Table II. Sections II B 1–II B 6 provide a brief introduction to each machine learning regression model and its hyperparameters used in this study.

1. Support vector machine (SVM)

SVM aims to find a hyperplane that minimizes the error while maximizing the margin. The hyperparameters tuned include the kernel, degree, C, and gamma. The kernel specifies the function used to map data into higher dimensions, with options such as linear, polynomial, and radial basis function (RBF) kernels enabling flexibility in capturing non-linear relationships. The degree is relevant for polynomial kernels, specifying the polynomial's order and influencing the complexity of the decision surface. The regularization parameter C controls the trade-off between maximizing the margin and minimizing training error, with larger values focusing on reducing error at the cost of generalization. The gamma parameter defines the influence of a single training sample, where higher values make the model sensitive to nearby points, potentially leading to overfitting.

2. Random forest (RF)

RF is an ensemble learning method that combines predictions from multiple decision trees to improve accuracy and reduce overfitting. It constructs each tree on a bootstrap sample of the dataset and selects a subset of features for splitting nodes, introducing

28 June 2025 08:06:18

TABLE I. List of descriptors and their corresponding explanations.

Descriptor set	Descriptor	Explanation
Property descriptors	T	Temperature (K)
	fheatcap	Specific heat capacity of the film (J/gK)
	fmelt	Melting point of the film (K)
	fdensity	Density of the film (g/cm ³)
	funit	Unit cell volume of the film (10 ⁻²⁹ m ³ /f.u.)
	fbm	Bulk modulus of the film (GPa)
	fsm	Shear modulus of the film (GPa)
	sheatcap	Specific heat capacity of the substrate (J/gK)
	smelt	Melting point of the substrate (K)
	sdensity	Density of the substrate (g/cm ³)
	sunit	Unit cell volume of the substrate (10 ⁻²⁹ m ³ /f.u.)
	sbm	Bulk modulus of the substrate (GPa)
	ssm	Shear modulus of the substrate (GPa)
Compound descriptors	fr1	Atomic ratio of the first element of the film
	fr2	Atomic ratio of the second element of the film
	fAC1x	AC represents atomic coordinates defined from the periodic table. The group as the x coordinate and the period as the y coordinate
	fAC1y	as (fACix, fACiy), where i represents the order of the elements of the film
	fAC2x	
	fAC2y	
	fmass	Mass of the film (u)
	fEb	Binding energy of the film (eV/f.u.)
	fENc	Electronegativity for cation of the film
	fENa	Electronegativity for anion of the film
	fIPc	Ionic potential for cation of the film
	fIPa	Ionic potential for anion of the film
	sR1	Atomic ratio of the first element of the substrate
	sR2	Atomic ratio of the second element of the substrate
	sAC1x	AC represents atomic coordinates defined from the periodic table. The group as the x coordinate and the period as the y coordinate
	sAC1y	as (sACix, sACiy), where i represents the order of the elements of the substrate
	sAC2x	
	sAC2y	
	smass	Mass of the substrate (u)
	sEb	Binding energy of the substrate (eV/f.u.)
	sENc	Electronegativity for cation of the substrate
	sENa	Electronegativity for anion of the substrate
	sIPc	Ionic potential for cation of the substrate
	sIPa	Ionic potential for anion of the substrate
Process descriptors	fthick	Film thickness (nm)
	interlayer	1 (exist) or 0 (absent)

randomness and diversity among trees. The prediction is the average of all tree outputs, formulated as

$$\hat{y} = \frac{1}{n} \sum_{i=1}^n T_i(x),$$

TABLE II. Hyperparameters for the representative machine learning models selected after five random splits of the dataset.

Algorithm	Hyperparameters
SVM	kernel = "poly," C = 100, degree = 9, gamma = 0.03
DT	max_depth = 9, min_samples_split = 3, min_samples_leaf = 1, max_features = 6
RF	n_estimators = 121, max_depth = 12, max_features = 39
GBDT	n_estimators = 326, max_depth = 5, max_features = 8, min_samples_split = 5, min_samples_leaf = 1
GP	kernel = RBF (1.0), alpha = 0.1
NN	hidden_layer_sizes = (5, 18), alpha = 0.0001
Descriptor-selected RF	n_estimators = 19, max_depth = 9, max_features = 3
Descriptor-redefined RF	n_estimators = 9, max_depth = 12, max_features = 3

where $T_i(x)$ is the prediction from the i th tree and n is the total number of trees. The hyperparameters selected for tuning include $n_estimators$, max_depth , and $max_features$. The $n_estimators$ defines the number of trees in the ensemble, with a higher number generally reducing variance at the cost of increased computational complexity. The max_depth restricts the depth of individual trees, serving as a control for overfitting by limiting tree complexity. The $max_features$ determines the number of descriptors considered for splitting at each node, where lower values introduce greater randomness, enhancing generalization.

3. Decision tree (DT)

DT splits the input space into regions based on learned hierarchical rules, with each region corresponding to a leaf node where the prediction is the average of the target values of the samples in that region. The hyperparameters adjusted include the max_depth , $min_samples_split$, $min_samples_leaf$, and $max_features$. The max_depth restricts the depth of the tree, controlling its capacity to fit the data and mitigating overfitting. The $min_samples_split$ determines the minimum number of samples required to split a node, reducing the risk of splits on small subsets. The $min_samples_leaf$ specifies the minimum number of samples in a leaf node, preventing overly small and unstable terminal nodes. The $max_features$ controls the number of descriptors considered for each split, where smaller values enhance randomness and reduce the risk of overfitting.

4. Gradient boosting decision tree (GBDT)

GBDT is a boosting algorithm that iteratively trains weak learners, typically decision trees, to minimize residual errors from the previous iteration. The hyperparameters considered for tuning include the $n_estimators$, max_depth , $max_features$, $min_samples_split$, and $min_samples_leaf$. The $n_estimators$ defines the number of boosting stages, where more stages can improve

28 June 2025 08:06:18

accuracy at the cost of increased overfitting risk. The `max_depth` restricts the depth of individual trees, balancing model complexity and generalization. The `max_features` specifies the number of descriptors considered for splits, with lower values introducing diversity to the ensemble. The `min_samples_split` defines the minimum number of samples required to split an internal node, reducing overfitting by discouraging splits on small subsets. The `min_samples_leaf` ensures that each terminal node contains a minimum number of samples, preventing overly fine partitions that can degrade generalization.

5. Gaussian process (GP)

GP is a non-parametric Bayesian approach that models the distribution of functions using a kernel function to define the covariance between points. The hyperparameters selected for optimization include the kernel, length scale, and alpha. The kernel determines the covariance function, with the Radial Basis Function kernel being a popular choice for smooth and flexible predictions. The length scale controls the extent of influence that a data point has on predictions, where larger values result in smoother functions. The alpha parameter serves as a regularization term, stabilizing the solution and improving model performance on noisy or poorly conditioned datasets.

6. Neural network (NN)

NN is a computational model inspired by biological neural systems, consisting of layers of interconnected neurons. Each neuron applies a weighted sum of inputs, followed by an activation function. The weights are optimized during training by minimizing the loss function through backpropagation and gradient descent. The hyperparameters adjusted include the `hidden_layer_sizes` and alpha. The `hidden_layer_sizes` defines the network's capacity to model complex patterns, with deeper or wider networks capturing more intricate relationships but increasing the risk of overfitting. The alpha parameter is a regularization factor added to the loss function to penalize large weights, thereby reducing overfitting and enhancing generalization.

III. RESULTS AND DISCUSSION

A. Accuracy of machine learning models

Six machine learning algorithms, namely, SVM, DT, RF, GBDT, GP, and NN, were employed for constructing machine learning models of ITR. The performance of the machine learning models was assessed by the Pearson correlation coefficient (R), the coefficient of determination (R^2), and the root mean square error (RMSE). The average evaluation results of the six models across five random dataset splits are presented in Table III. The accuracy of all six models on the training dataset is significantly high, with R values above 0.96 and R^2 values above 0.93, indicating their ability to capture the underlying relationships in the data. For the testing dataset, the models show comparable and slightly lower accuracy, with R values above 0.94 and R^2 values exceeding 0.89, suggesting the good generalization performance. To mitigate overfitting, five-fold cross-validation was employed during model training. The differences in testing dataset performance highlight the varying

degrees of generalization among the six algorithms. Among the six models, the RF model exhibits the highest R (0.971) and R^2 (0.940) for the testing dataset and the lowest RMSE ($7.909 \times 10^{-9} \text{ m}^2 \text{ K/W}$), making it the best-performing machine learning algorithm. The GBDT model possesses a similarly high level of accuracy, with $R = 0.970$, $R^2 = 0.938$, and $\text{RMSE} = 8.046 \times 10^{-9} \text{ m}^2 \text{ K/W}$. In comparison, the SVM and DT models exhibit comparable accuracy that is slightly lower than that of the RF and GBDT models. Although the NN ($R = 0.949$, $R^2 = 0.898$, and $\text{RMSE} = 10.856 \times 10^{-9} \text{ m}^2 \text{ K/W}$) and GP ($R = 0.951$, $R^2 = 0.897$, and $\text{RMSE} = 9.388 \times 10^{-9} \text{ m}^2 \text{ K/W}$) models show the lowest performance, they still present reasonable accuracy in describing ITR. Moreover, the RF and GBDT models are all more accurate than previous results.^{38,53} Among the five random splits of the dataset, most algorithms demonstrate minimal variation in model performance, except for the NN model. Due to its sensitivity to hyperparameter tuning, the NN model exhibits slightly larger performance fluctuations.

For each algorithm, a representative model was selected, and its performance is illustrated in Fig. 2. The results show that the predicted values closely align with the experimental values, with data points distributed near the diagonal line on the testing dataset, indicating high prediction accuracy. The performance ranking of the models is as follows: RF > GBDT > NN > DT > SVM > GP. Among these, the RF model consistently achieves the best evaluation metrics, highlighting its superiority in the task of ITR prediction.

The RF algorithm, by combining multiple decision trees and aggregating their predictions, mitigates the overfitting issue and achieves robust results on both the training and testing datasets.⁵⁴ Consequently, it has demonstrated a high accuracy in dealing with a variety of physical and chemical problems.^{55,56} Moreover, the RF algorithm provides a measure of feature importance that indicates the relative contribution of each input variable to the prediction task. This information is particularly important in understanding the underlying data patterns and selecting relevant descriptors for future modeling endeavors. Therefore, the RF algorithm is chosen for subsequent descriptor selection procedures.

B. Feature engineering

Feature engineering aims to construct informative and discriminative descriptors from raw data to improve the performance of machine learning models. The feature engineering process employed in this study is outlined in Fig. 1(c). Initially, descriptors were screened based on their mutual correlations and importance rankings derived from the RF algorithm. Descriptors with low inter-descriptor correlations and high importance scores were retained, reducing the original set of 39 descriptors to 7. Subsequently, by analyzing the physical properties of these seven descriptors, a new descriptor representing the degree of sound velocity matching was defined and incorporated into the descriptor set. After further refinement, the final descriptor set was reduced to six descriptors. The specific descriptor selection process is detailed as follows.

Highly correlated descriptors can lead to information redundancy, and some descriptors may be unrelated to ITR, thereby reducing the accuracy of the model. To select the most relevant descriptors, we calculated the spearman correlation coefficients

28 June 2025 08:06:18

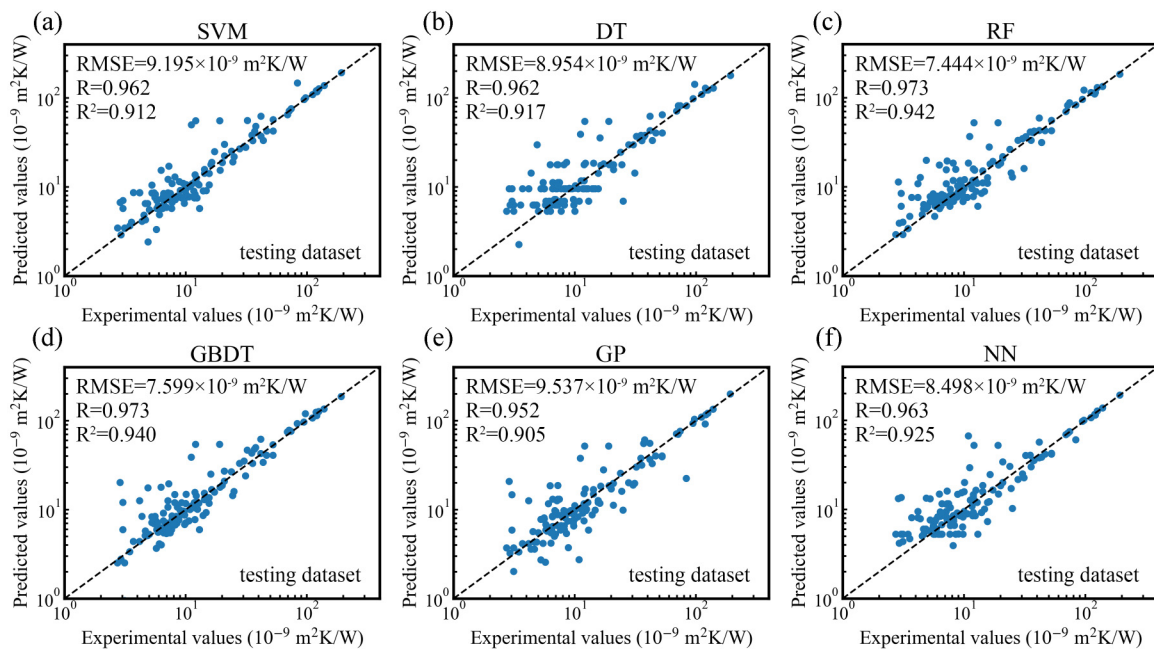
TABLE III. The average prediction accuracies of the machine learning algorithms over five random dataset splits.

Algorithm	R (training)	R ² (training)	RMSE (training)	R (testing)	R ² (testing)	RMSE (testing)
SVM	0.983	0.966	5.733	0.958	0.917	9.082
DT	0.990	0.980	4.350	0.959	0.918	9.021
RF	0.988	0.977	4.740	0.971	0.940	7.909
GBDT	0.992	0.985	3.796	0.970	0.938	8.046
GP	0.986	0.970	5.441	0.951	0.897	9.388
NN	0.965	0.931	7.982	0.949	0.898	10.856
Descriptor-selected RF	0.988	0.976	4.754	0.971	0.940	7.646
Descriptor-redefined RF	0.989	0.976	4.875	0.971	0.942	7.133

among the 39 descriptors, as shown in Fig. 3. The blue and red colors represent positive and negative correlations, respectively. Based on the Spearman correlation coefficient matrix, pairs of descriptors with absolute correlation coefficients greater than 0.8 were considered strongly correlated.^{57,58} Descriptors exhibiting strong mutual correlations were assigned to the same group, resulting in a total of 12 descriptor groups, which are (fheatcap, fmass, fAC1y, fAC2y, fdensity, fIPc, fIPa, fENc, and fENa), (sunit, sIPc, sENc, sAC1x, sAC2x, smass, sENa, sIPa, sEb, sR2, sAC2y, and sR1), (fmelt, fEb, fAC1x, fAC2x, and fbm), (smelt, sbm, and ssm), (T and sheatcap), (fR1 and fR2), (interlayer), (fthick), (funit), (sdensity), (sAC1y), and (fsm), respectively. Within each group, the descriptors were highly correlated,

allowing using one descriptor to represent the information of the entire group.

Figure 4 shows the feature importance in the RF model, which quantitatively describes the contribution of descriptors to the model. The higher a descriptor's importance score, the greater the role that descriptor plays in the model's prediction. The results show that some of the 39 descriptors contribute very little to the model, which may be because these descriptors have a low correlation with thermal conductivity, or other descriptors already adequately capture information in the data. By further considering the feature importance, we selected one descriptor that is most important within each group. The screened 12 descriptors are, in descending importance order, fbm (bulk modulus of the film), fheatcap

**FIG. 2.** Comparison of predicted ITR values and experimental values for the testing dataset using representative models from six machine learning algorithms: (a) SVM, (b) DT, (c) RF, (d) GBDT, (e) GP, and (f) NN. Each representative model was selected after five random splits of the dataset. Dashed lines indicate the ideal prediction ($y = x$), serving as visual references for model accuracy.

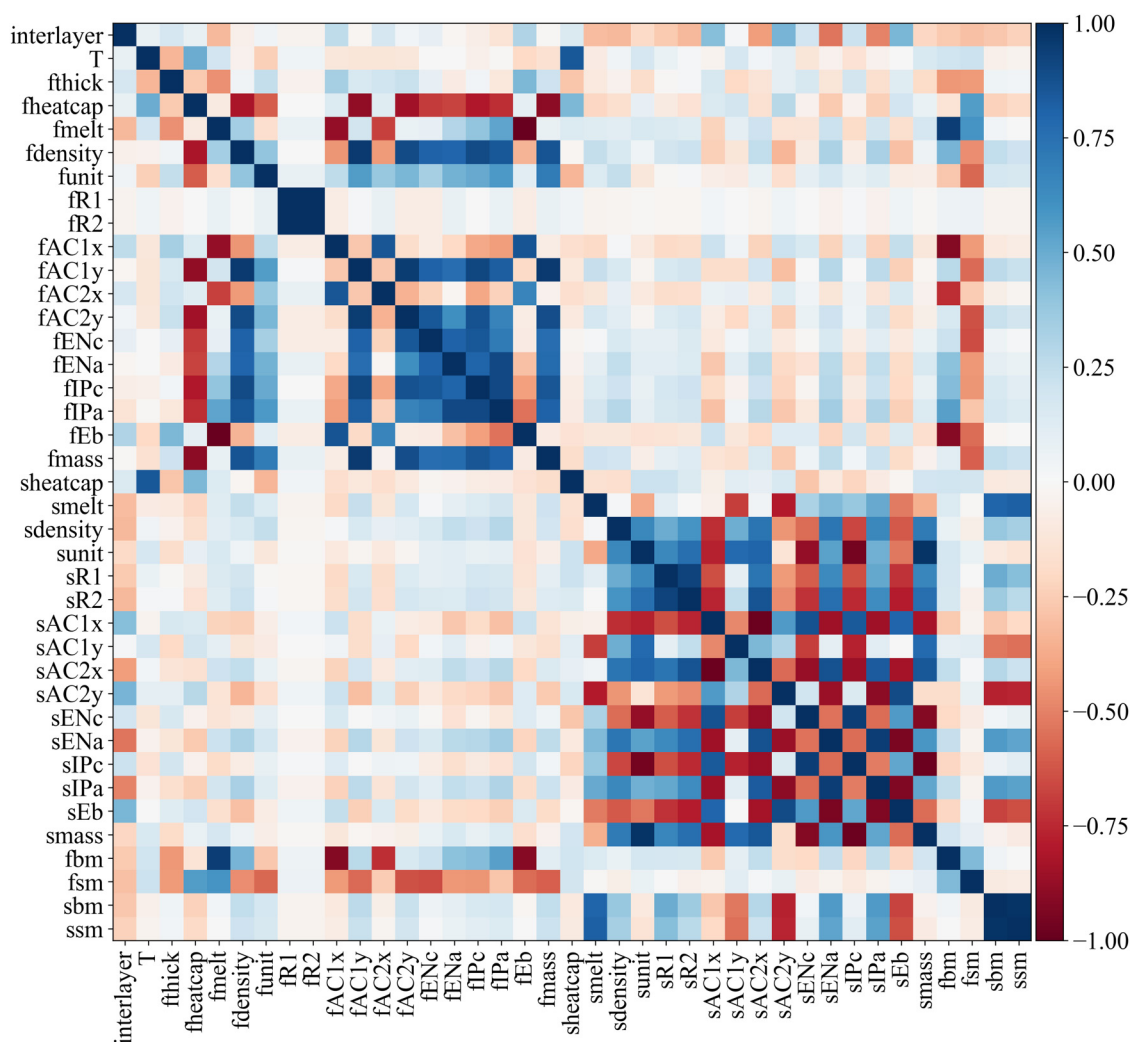


FIG. 3. Spearman correlation coefficients between the 39 raw descriptors.

(specific heat capacity of the film), sheatcap (specific heat capacity of the substrate), fthick (film thickness), fsm (shear modulus of the film), smelt (melting point of the substrate), smass (mass of the substrate), funit (volume per formula unit of the film), sAC1y (the periodic coordinates defined from the periodic table of the first element of the substrate), interlayer (the presence of an interlayer), sdensity (density of the substrate), and fR2 (atomic ratio of the second element of the film). While the correlations among these descriptors are relatively low, the latter six descriptors exhibit substantially low importance. Therefore, we retained only the top six descriptors with the highest feature importance (fbm, fheatcap, sheatcap, fsm, fthick, and smelt), including the material properties of both the film and the substrate. Besides, interlayer as a process descriptor is also needed in constructing machine learning models.

Table III presents the average evaluation results across five random dataset splits. The results indicate that the RF model constructed using the selected seven descriptors achieves an average performance on the testing dataset of $R = 0.971$, $R^2 = 0.940$, and $RMSE = 7.646 \times 10^{-9} \text{ m}^2 \text{ K/W}$. Compared to the RF model built with all 39 raw descriptors ($RMSE = 7.909 \times 10^{-9} \text{ m}^2 \text{ K/W}$), the descriptor-selected RF model demonstrates higher accuracy. The variation in evaluation metrics among the five splits is minimal, further validating the robustness of the descriptor selection process. The performance of the representative descriptor-selected RF model is illustrated in Fig. 5, where data points from both the training and testing datasets are distributed near the diagonal line. This distribution confirms the high predictive accuracy of the descriptor-selected RF model.

28 June 2025 08:06:18

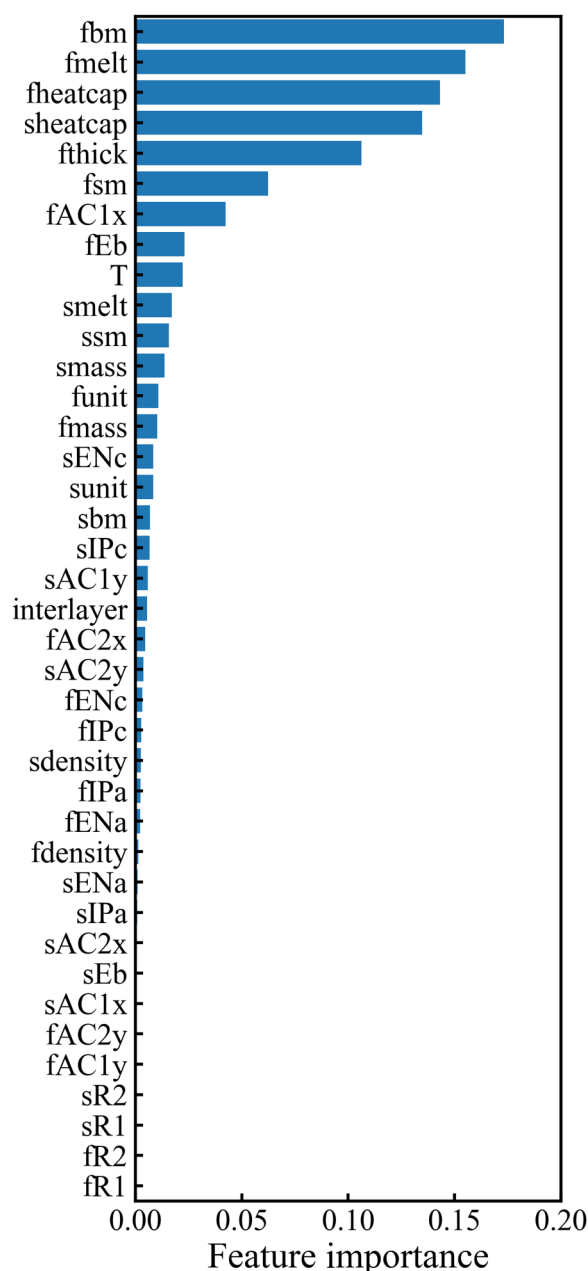


FIG. 4. Feature importance ranking for all the 39 descriptors obtained from the representative RF model.

C. Feature importance and physical insights

Machine learning algorithms have demonstrated considerable accuracy in predicting ITR, but their lack of interpretability due to being black-box processes makes it difficult to clarify the underlying mechanisms. Therefore, it is crucial to extract physical information from the machine learning process, and analyzing important

descriptors can provide scientific insights. In the descriptor-selected RF model, only seven descriptors were retained, including two process descriptors (interlayer and fthick) and five property descriptors (fheatcap, fbm, fsm, sheatcap, and smelt). The Spearman correlation heat map of the seven descriptors shows low correlations among them [Fig. 6(a)].

In addition, we also apply the SHapley Additive exPlanations (SHAP) algorithm to analyze the influence of the selected descriptors on the RF model. SHAP is a unified framework based on game theory that assigns each descriptor an importance value by interpreting the contribution of the descriptor to predictions, ensuring consistency and fairness in descriptor attribution. Figure 6(b) shows the SHAP-based representation of feature importance, whose values refer to the average SHAP values. The results show that, except for the interlayer descriptor, the other six descriptors all show high descriptor importance, which reflects the effectiveness of the previous descriptor screening method.

From the perspective of heat transfer, this result is readily understandable because all these property descriptors are strongly related to heat conduction across the interfaces. Specifically, the elastic modulus, heat capacity, and melting point are closely related to the bonding strength between atoms, which essentially determines heat conduction in crystals and that across interfaces. The crystals with larger elastic modulus often have higher group velocities and, thus, higher lattice thermal conductivity. Based on the current understanding of interfacial thermal transport, interfacial thermal resistance strongly depends on the matching degree of the vibrational properties of two materials forming the interface, namely, a larger mismatch results in larger ITR, and vice versa.³ Essentially, AMM, DMM, and similar models quantify the ITR by calculating the mismatch of vibrational properties in different ways. The ratio of elastic modulus has been used as a metric of this mismatch, but its effectiveness is not always guaranteed.^{59–61} It is noted that the feature engineering selects three descriptors for the film and two descriptors for the substrate, indicating that the mismatch between them is included into the machine learning model. We, therefore, define two new descriptors $LV = \sqrt{bm}/\text{density}$ and $TV = \sqrt{sm}/\text{density}$ and use the ratios of $LV (= fLV/sLV$ or sLV/fLV if $fLV > sLV$) and $TV (= fTV/sTV$ or sTV/fTV if $fTV > sTV$) as a metric for the mismatch of vibrational properties. Here, fLV (sLV) and fTV (sTV) correspond to the longitudinal and transverse sound velocity of the film (substrate), respectively. In Figs. 7(a) and 7(b), we plot the interfacial thermal resistance used in the present study as a function of the ratios of LV and TV for the two materials at the interface. It can be seen that, in general, the interfacial thermal resistance decreases as the ratio increases, indicating that larger mismatch of sound velocity results in larger ITR. This observation allows good interpretability for our machine learning model. Note that, as a black box, the machine learning model describes the ITR in a more complicated form. In addition to the matching degree of LV and TV , there are many other factors affecting ITR, such as melting point, specific heat capacity, Debye temperature, atomic mass, local phonon density of states, and interfacial coordination number density.^{10,11,60,62,63} That is why the ITR can vary a lot for the interfaces with the same ratio of fLV/sLV or fTV/sTV . Furthermore, we compared the newly introduced descriptors with the elastic modulus ratio (fbm/sbm and fsm/ssm) by

28 June 2025 08:06:18

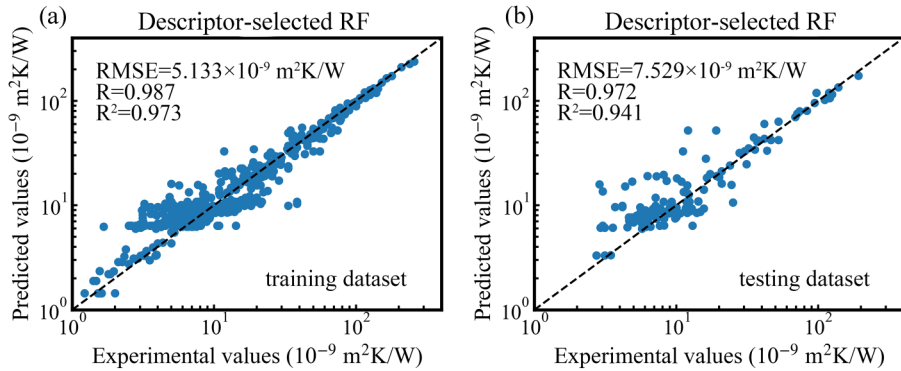


FIG. 5. Comparison between the predicted values by the representative RF model and the experimental values for the (a) training dataset and (b) testing dataset after the descriptor selection.

evaluating their Spearman correlation coefficients with ITR. As shown in Fig. 7(c), The LV and TV ratios exhibit significantly stronger correlations with ITR than either modulus ratios, highlighting their superiority in representing the vibrational mismatch across interfaces.

Because the ITR strongly depends on the mismatch of LV and TV, we subsequently retrained the RF model using a new set of descriptors including interlayer, fthick, fheatcap, sheatcap, and the ratios of LV and TV. We evaluated the correlations among these descriptors, as shown in Fig. 7(d), and found that the ratios of LV and TV are highly correlated with each other. Typically, longitudinal phonons dominate thermal transport across smooth and well-matched interfaces while transverse phonons become significant in rough or disordered interfaces, where diffuse scattering enables partial transmission. Therefore, although they are statistically correlated, both descriptors were retained in the model to reflect their distinct physical significance. During model training, we performed an independent grid search combined with fivefold cross-validation. The hyperparameter values of the descriptor-redefined RF model were selected based on the best average cross-validation performance. Table III shows the average evaluation results of the descriptor-redefined RF model across five random dataset splits, while the performance of the representative model is illustrated in Figs. 8(a) and 8(b). The results demonstrate that the descriptor-redefined RF model exhibits strong consistency between predicted

and experimental values on both the training and testing data sets, indicating high accuracy and robust generalization capability. The evaluation metrics of the descriptor-redefined RF model on the testing dataset are $R = 0.971$, $R^2 = 0.942$, and $\text{RMSE} = 7.133 \times 10^{-9} \text{ m}^2 \text{K/W}$, which are slightly better than those of the descriptor-selected RF model and the original RF model. Figure 8(c) presents the feature importance derived from SHAP analysis, while Fig. 8(d) displays the SHAP beeswarm plot. In the beeswarm plot, each point's color indicates the magnitude of its original eigenvalue, and its position on the X axis represents its SHAP value, indicating the positive or negative impact on the model's predicted value. As shown in Figs. 8(c) and 8(d), the redefined descriptors, the ratio of LV and the ratio of TV, exhibit the highest SHAP feature importance. Moreover, smaller the ratio of LV and the ratio of TV are associated with larger ITR values, highlighting the reliability of the redefined descriptors.

D. Application of the machine learning model

Machine learning-based predictions provide a multidimensional material design space, offering an alternative approach to explore interfacial thermal resistance with shorter time frames and reduced variability compared to traditional experimental processes. We next employed the RF model to explore the materials that have a low ITR with the electronic chip material of Si (here defined as a

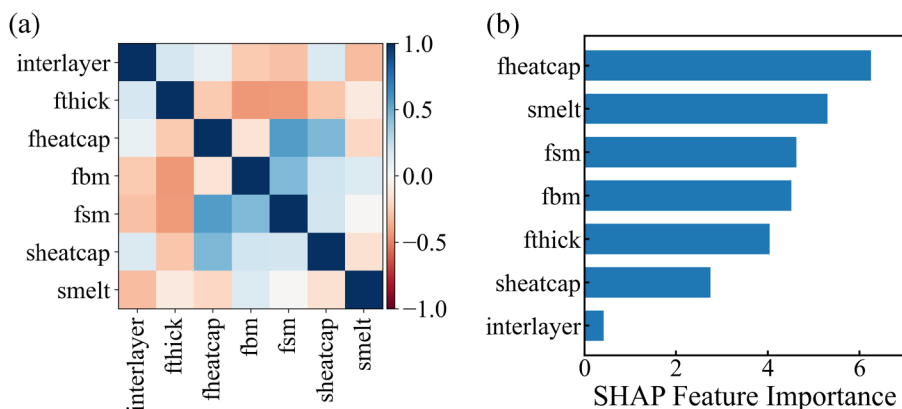


FIG. 6. (a) Spearman correlation coefficients of the remaining seven descriptors after the descriptor selection step. (b) SHAP feature importance ranking provided in the representative descriptor-selected RF model.

28 June 2025 08:06:18

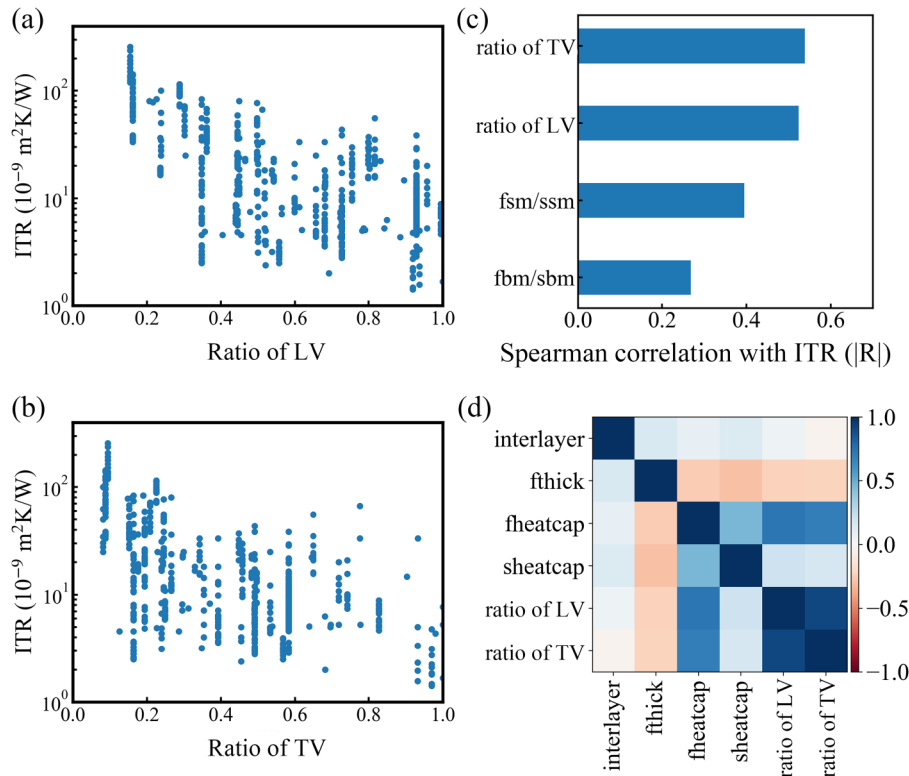


FIG. 7. The distribution of ITR with respect to (a) the ratios of LV (= f_{LV}/s_{LV} or s_{LV}/f_{LV} if $f_{LV} > s_{LV}$) and (b) TV (= f_{TV}/s_{TV} or s_{TV}/f_{TV} if $f_{TV} > s_{TV}$) of two materials at the interface in the original dataset. Here, f_{LV} (s_{LV}) and f_{TV} (s_{TV}) correspond to the longitudinal and transverse sound velocity of the film (substrate), respectively. (c) Spearman correlation analysis between ITR and four descriptors related to vibrational mismatch. (d) Spearman correlation heatmap for six descriptors used in the descriptor-redefined RF model.

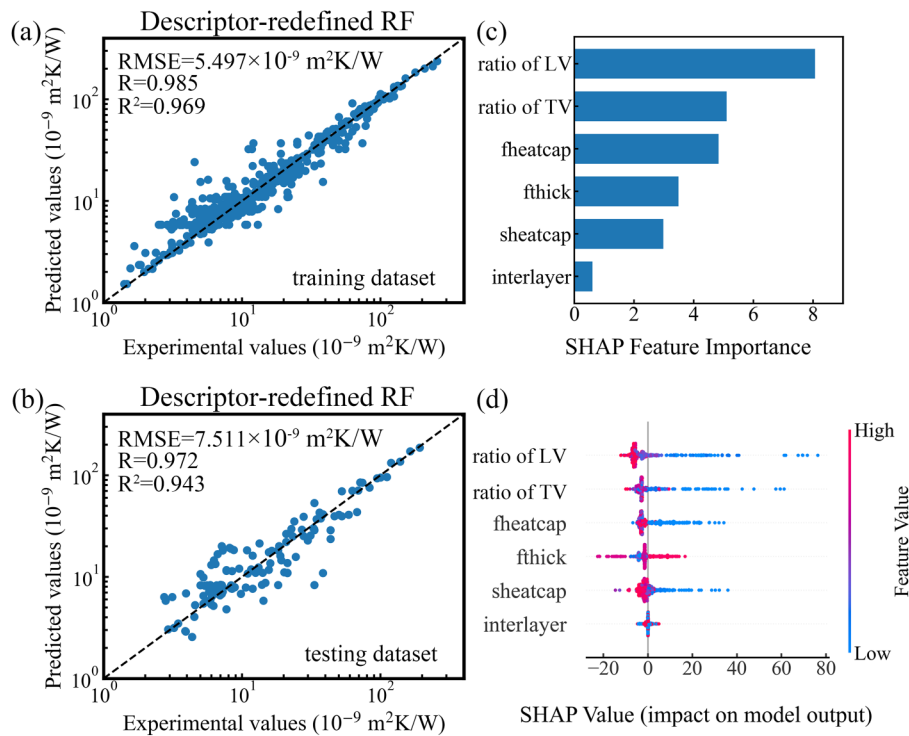


FIG. 8. Comparison between the predicted values by the representative RF model and the experimental values for the (a) training and (b) testing dataset. (c) SHAP feature importance ranking provided in the representative descriptor-redefined RF model. (d) SHAP summary plot analysis for the training dataset showing the impact of descriptors on the representative descriptor-redefined RF model.

28 June 2025 08:06:18

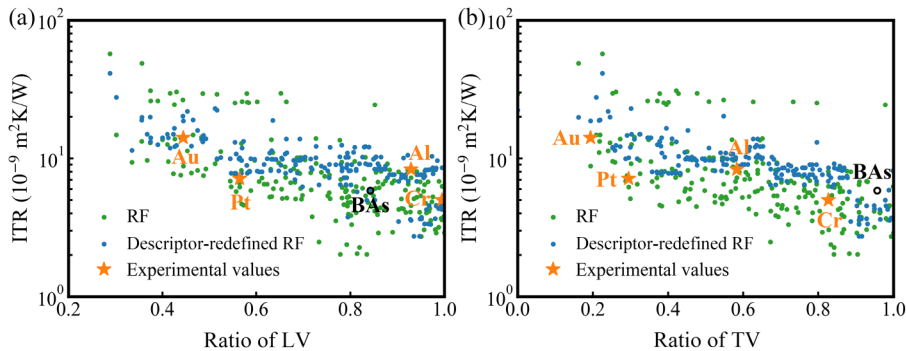


FIG. 9. The predicted ITR distribution with respect to (a) the ratios of LV ($= fLV/sLV$ or sLV/fLV if $fLV > sLV$) and (b) TV ($= fTV/sTV$ or sTV/fTV if $fTV > sTV$) of two materials at the interface. The settings of interlayer, T, and θ are 0, 300 K, and 30 nm, respectively. The stars represent the experimental values in the original dataset. The open circles represent the ITR of the BAs/Si interface predicted by the representative descriptor-redefined RF model.

typical substrate). Specifically, we predicted the ITR for 202 different interfaces at 300 K by varying the film materials with a thickness of 30 nm and considering no interlayer. Figure 9 shows the predicted data with respect to the ratios of LV ($= fLV/sLV$ or sLV/fLV if $fLV > sLV$) and TV ($= fTV/sTV$ or sTV/fTV if $fTV > sTV$) of two materials at the interface. The predicted results from the RF model and descriptor-redefined RF model show the same trend, which further confirms the rationality of the descriptor selection. The results show that the ITR has a negative correlation with the matching degree of LV and TV of two materials at the interface. An interface with a high matching degree of LV (or TV), i.e., the ratio of LV (or TV) is close to 1, exhibits a relatively low ITR. For example, the ratios of LV (0.995) and TV (0.827) are much higher for the Cr/Si interface than that (0.445 and 0.194) for the Au/Si case, and correspondingly, the ITR of the former is predicted to be much lower than the latter. As expected, some interfaces (such as Pt/Si and Al/Si) deviate from this general trend, e.g., the ITR of Pt/Si is lower than that of Al/Si, while the mismatch of LV and TV is larger for Pt/Si. This deviation indicates other factors play significant roles in determining interfacial thermal transport, e.g., the interfacial quality (roughness, defects, etc.) of Al/Si may be poor, resulting in increased ITR. In general, one can expect the machine learning model provides reliable prediction for those with good sample quality and interfacial conditions.

Finally, we made a prediction for cubic BAs, a material that has garnered significant attention because of its ultrahigh thermal conductivity and carrier mobility. The prediction results indicate that the ITR at the BAs/Si interface is merely $5.86 \times 10^{-9} \text{ m}^2 \text{ K/W}$, which is very close to the result of MD calculation of about $4.44 \times 10^{-9} \text{ m}^2 \text{ K/W}$.⁶⁴ Such low ITR of BAs/Si interface underscores the exceptional ability of BAs to facilitate rapid heat dissipation in Si chip devices. The super heat-conducting material BAs, which possesses both high thermal conductivity and low ITR, exhibits vast potential for applications in thermal management of electronics.

IV. CONCLUSION

In summary, we have established six machine learning models to describe the ITR of metal/non-metal and non-metal/non-metal interfaces and achieved the highest accuracy for the RF model. Using the RF model, we implemented feature engineering to eliminate redundancy from the original 39 descriptors and identified 7

most relevant descriptors, without sacrificing the accuracy of models. Among them, five property descriptors are all strongly related to the bonding strength and, thus, the vibrational properties of the two materials at the interface. In particular, we have defined new descriptors corresponding to the matching degree of the sound velocity, achieving an improved RF model. The key physical descriptors identified here improve the interpretability of the machine learning models, which can serve as an efficient tool for the design and optimization of thermal interfaces in relevant applications.

Taking Si as an example, we applied the developed machine learning model to explore the materials that can achieve a low ITR with Si. In particular, our prediction indicates that the ITR of the BAs/Si interface is relatively low among the 202 interfaces, suggesting the potentials of using BAs for the efficient thermal management of electronics.

ACKNOWLEDGMENTS

This work was supported by the Excellent Young Scientists Fund (Overseas) of Shandong Province (Grant No. 2022HWYQ-091), the Taishan Scholars Program of Shandong Province (Grant No. tsqnz20221163), and the Natural Science Foundation of Shandong Province (Grant No. ZR2022MA011). Weidong Zheng acknowledges the support from Natural Science Foundation of Shandong Province (Grant No. ZR2023QE223) and the Taishan Scholars Program of Shandong Province (Grant No. tsqn202312294).

AUTHOR DECLARATIONS

Conflict of Interest

The authors have no conflicts to disclose.

Author Contributions

Xiaohan Song: Conceptualization (equal); Data curation (lead); Formal analysis (lead); Visualization (lead); Writing – original draft (lead). **Weidong Zheng:** Writing – review & editing (supporting). **Haoqiang Ai:** Writing – review & editing (supporting). **Hao Zhou:** Investigation (supporting). **Liyin Feng:** Investigation (supporting). **Zheng Cui:** Resources (equal); Software (equal). **Ruiqiang Guo:**

28 June 2025 08:06:18

Conceptualization (lead); Formal analysis (lead); Funding acquisition (lead); Resources (lead); Writing – review & editing (lead).

DATA AVAILABILITY

The data that support the findings of this study are available from the corresponding author upon reasonable request.

REFERENCES

- ¹D. G. Cahill, P. V. Braun, G. Chen, D. R. Clarke, S. Fan, K. E. Goodson, P. Keblinski, W. P. King, G. D. Mahan, A. Majumdar, H. J. Maris, S. R. Phillpot, E. Pop, and L. Shi, “Nanoscale thermal transport. II. 2003–2012,” *Appl. Phys. Rev.* **1**(1), 011305 (2014).
- ²A. L. Moore and L. Shi, “Emerging challenges and materials for thermal management of electronics,” *Mater. Today* **17**(4), 163 (2014).
- ³J. Chen, X. Xu, J. Zhou, and B. Li, “Interfacial thermal resistance: Past, present, and future,” *Rev. Mod. Phys.* **94**(2), 025002 (2022).
- ⁴H. Song, J. Liu, B. Liu, J. Wu, H.-M. Cheng, and F. Kang, “Two-dimensional materials for thermal management applications,” *Joule* **2**(3), 442 (2018).
- ⁵Y. Zhou, S. Wu, Y. Long, P. Zhu, F. Wu, F. Liu, V. Murugadoss, W. Winchester, A. Nautiyal, Z. Wang, and Z. Guo, “Recent advances in thermal interface materials,” *ES Mater. Manuf.* **7**, 4 (2020).
- ⁶K. Ruan, X. Shi, Y. Guo, and J. Gu, “Interfacial thermal resistance in thermally conductive polymer composites: A review,” *Compos. Commun.* **22**, 100518 (2020).
- ⁷L. Hu, T. Desai, and P. Keblinski, “Determination of interfacial thermal resistance at the nanoscale,” *Phys. Rev. B* **83**(19), 195423 (2011).
- ⁸H. Sun, R. B. Simon, J. W. Pomeroy, D. Francis, F. Faily, D. J. Twitchen, and M. Kuball, “Reducing GaN-on-diamond interfacial thermal resistance for high power transistor applications,” *Appl. Phys. Lett.* **106**(11), 111906 (2015).
- ⁹T. Feng, H. Zhou, Z. Cheng, L. S. Larkin, and M. R. Neupane, “A critical review of thermal boundary conductance across wide and ultrawide bandgap semiconductor interfaces,” *ACS Appl. Mater. Interfaces* **15**(25), 29655 (2023).
- ¹⁰H. S. Park and J. Punch, “Friction factor and heat transfer in multiple microchannels with uniform flow distribution,” *Int. J. Heat Mass Transfer* **51**(17), 4535 (2008).
- ¹¹E. T. Swartz and R. O. Pohl, “Thermal boundary resistance,” *Rev. Mod. Phys.* **61**(3), 605 (1989).
- ¹²R. S. Prasher and P. E. Phelan, “A scattering-mediated acoustic mismatch model for the prediction of thermal boundary resistance,” *J. Heat Transfer* **123**(1), 105 (2000).
- ¹³R. Prasher, “Acoustic mismatch model for thermal contact resistance of van der Waals contacts,” *Appl. Phys. Lett.* **94**(4), 041905 (2009).
- ¹⁴H. Wang, Y. Xu, M. Shimono, Y. Tanaka, and M. Yamazaki, “Computation of interfacial thermal resistance by phonon diffuse mismatch model,” *Mater. Trans.* **48**(9), 2349 (2007).
- ¹⁵T. Zhan, L. Fang, and Y. Xu, “Prediction of thermal boundary resistance by the machine learning method,” *Sci. Rep.* **7**(1), 7109 (2017).
- ¹⁶E. S. Landry and A. J. H. McGaughey, “Thermal boundary resistance predictions from molecular dynamics simulations and theoretical calculations,” *Phys. Rev. B* **80**(16), 165304 (2009).
- ¹⁷Q. Song and G. Chen, “Evaluation of the diffuse mismatch model for phonon scattering at disordered interfaces,” *Phys. Rev. B* **104**(8), 085310 (2021).
- ¹⁸H. Bao, J. Chen, X. Gu, and B. Cao, “A review of simulation methods in micro/nanoscale heat conduction,” *ES Energy Environ.* **1**, 16 (2018).
- ¹⁹S. Zhai, P. Zhang, Y. Xian, J. Zeng, and B. Shi, “Effective thermal conductivity of polymer composites: Theoretical models and simulation models,” *Int. J. Heat Mass Transfer* **117**, 358 (2018).
- ²⁰S. Xiong, B. Latour, Y. Ni, S. Volz, and Y. Chalopin, “Efficient phonon blocking in SiC antiphase superlattice nanowires,” *Phys. Rev. B* **91**(22), 224307 (2015).
- ²¹Y. Cheng, Z. Fan, T. Zhang, M. Nomura, S. Volz, G. Zhu, B. Li, and S. Xiong, “Magic angle in thermal conductivity of twisted bilayer graphene,” *Mater. Today Phys.* **35**, 101093 (2023).
- ²²Z. Wei, Z. Ni, K. Bi, M. Chen, and Y. Chen, “Interfacial thermal resistance in multilayer graphene structures,” *Phys. Lett. A* **375**(8), 1195 (2011).
- ²³H. Zhong and J. R. Lukes, “Interfacial thermal resistance between carbon nanotubes: Molecular dynamics simulations and analytical thermal modeling,” *Phys. Rev. B* **74**(12), 125403 (2006).
- ²⁴K. Ren, X. Liu, S. Chen, Y. Cheng, W. Tang, and G. Zhang, “Remarkable reduction of interfacial thermal resistance in nanophononic heterostructures,” *Adv. Funct. Mater.* **30**(42), 2004003 (2020).
- ²⁵J.-S. Wang, J. Wang, and N. Zeng, “Nonequilibrium Green’s function approach to mesoscopic thermal transport,” *Phys. Rev. B* **74**(3), 033408 (2006).
- ²⁶J. Lee, A. K. Roy, and B. L. Farmer, “Kapitza resistance in the lattice Boltzmann-Peierls-Callaway equation for multiphase phonon gases,” *Phys. Rev. E* **83**(5), 056706 (2011).
- ²⁷K. T. Butler, D. W. Davies, H. Cartwright, O. Isayev, and A. Walsh, “Machine learning for molecular and materials science,” *Nature* **559**(7715), 547 (2018).
- ²⁸H. Zhang, K. Hippalgaonkar, T. Buonassisi, O. M. Løvvik, E. Sagvolden, and D. Ding, “Machine learning for novel thermal-materials discovery: Early successes, opportunities, and challenges,” *ES Energy Environ.* **2**, 1 (2018).
- ²⁹Y. Ouyang, C. Yu, G. Yan, and J. Chen, “Machine learning approach for the prediction and optimization of thermal transport properties,” *Front. Phys.* **16**(4), 43200 (2021).
- ³⁰S. Ju, S. Shimizu, and J. Shiomi, “Designing thermal functional materials by coupling thermal transport calculations and machine learning,” *J. Appl. Phys.* **128**(16), 161102 (2020).
- ³¹B. Mortazavi, E. V. Podryabinkin, S. Roche, T. Rabczuk, X. Zhuang, and A. V. Shapeev, “Machine-learning interatomic potentials enable first-principles multiscale modeling of lattice thermal conductivity in graphene/borophene heterostructures,” *Mater. Horiz.* **7**(9), 2359 (2020).
- ³²P. Roy Chowdhury and X. Ruan, “Unexpected thermal conductivity enhancement in aperiodic superlattices discovered using active machine learning,” *npj Comput. Mater.* **8**(1), 12 (2022).
- ³³Y. Luo, M. Li, H. Yuan, H. Liu, and Y. Fang, “Predicting lattice thermal conductivity via machine learning: A mini review,” *npj Comput. Mater.* **9**(1), 4 (2023).
- ³⁴Y. Liu, H. Liang, L. Yang, G. Yang, H. Yang, S. Song, Z. Mei, G. Csányi, and B. Cao, “Unraveling thermal transport correlated with atomistic structures in amorphous gallium oxide via machine learning combined with experiments,” *Adv. Mater.* **35**(24), e2210873 (2023).
- ³⁵Y.-B. Liu, J.-Y. Yang, G.-M. Xin, L.-H. Liu, G. Csányi, and B.-Y. Cao, “Machine learning interatomic potential developed for molecular simulations on thermal properties of β -Ga₂O₃,” *J. Chem. Phys.* **153**(14), 144501 (2020).
- ³⁶H. Yang, Z. T. Zhang, J. C. Zhang, and X. C. Zeng, “Machine learning and artificial neural network prediction of interfacial thermal resistance between graphene and hexagonal boron nitride,” *Nanoscale* **10**(40), 19092 (2018).
- ³⁷Y. Guo, G. Li, T. Mabuchi, D. Surblys, T. Ohara, and T. Tokumasu, “Prediction of nanoscale thermal transport and adsorption of liquid containing surfactant at solid-liquid interface via deep learning,” *J. Colloid Interface Sci.* **613**, 587 (2022).
- ³⁸Y.-J. Wu, L. Fang, and Y. Xu, “Predicting interfacial thermal resistance by machine learning,” *npj Comput. Mater.* **5**(1), 56 (2019).
- ³⁹Y. Liu, W. Zheng, H. Ai, L. Cheng, R. Guo, and X. Song, “Predicting the thermal conductivity of polymer composites with one-dimensional oriented fillers using the combination of deep learning and ensemble learning,” *Energy AI* **18**, 100445 (2024).
- ⁴⁰Y. Liu, W. Zheng, H. Ai, H. Zhou, L. Feng, L. Cheng, R. Guo, and X. Song, “Application of machine learning in predicting the thermal conductivity of single-filler polymer composites,” *Mater. Today Commun.* **39**, 109116 (2024).
- ⁴¹Y. Chen, S. Wang, J. Xiong, G. Wu, J. Gao, Y. Wu, G. Ma, H.-H. Wu, and X. Mao, “Identifying facile material descriptors for Charpy impact toughness

28 June 2025 08:06:18

in low-alloy steel via machine learning,” *J. Mater. Sci. Technol.* **132**, 213 (2023).

⁴²C. Shang, D. Zhu, H.-H. Wu, P. Bai, F. Hou, J. Li, S. Wang, G. Wu, J. Gao, X. Zhou, T. Lookman, and X. Mao, “A quantitative relation for the ductile-brittle transition temperature in pipeline steel,” *Scr. Mater.* **244**, 116023 (2024).

⁴³D. Zhu, H.-H. Wu, F. Hou, J. Zhang, Z. Gao, C. Shang, S. Wang, G. Wu, J. Gao, K. Pan, L. Hou, J. Ma, T. Lookman, and X. Mao, “A transfer learning strategy for tensile strength prediction in austenitic stainless steel across temperatures,” *Scr. Mater.* **251**, 116210 (2024).

⁴⁴F. Gou, Z. Ma, Q. Yang, H. Du, Y. Li, Q. Zhang, W. You, Y. Chen, Z. Du, J. Yang, N. He, J. Luo, Z. Liu, Z. Tian, M. Mao, K. Liu, J. Yu, A. Zhang, F. Min, K. Sun, and N. Xuan, “Machine learning-assisted prediction and control of bandgap for organic-inorganic metal halide perovskites,” *ACS Appl. Mater. Interfaces* **17**(12), 18383 (2025).

⁴⁵R. Jacobs, J. Liu, H. Abernathy, and D. Morgan, “Machine learning design of perovskite catalytic properties,” *Adv. Energy Mater.* **14**(12), 2303684 (2024).

⁴⁶X. Huang, S. Ma, C. Y. Zhao, H. Wang, and S. Ju, “Exploring high thermal conductivity polymers via interpretable machine learning with physical descriptors,” *npj Comput. Mater.* **9**(1), 191 (2023).

⁴⁷X. Huang, C. Y. Zhao, H. Wang, and S. Ju, “AI-assisted inverse design of sequence-ordered high intrinsic thermal conductivity polymers,” *Mater. Today Phys.* **44**, 101438 (2024).

⁴⁸Y.-J. Wu, T. Zhan, Z. Hou, L. Fang, and Y. Xu, “Physical and chemical descriptors for predicting interfacial thermal resistance,” *Sci. Data* **7**(1), 36 (2020).

⁴⁹Y. J. Wu, M. Sasaki, M. Goto, L. Fang, and Y. B. Xu, “Electrically conductive thermally insulating Bi-Si nanocomposites by interface design for thermal management,” *ACS Appl. Nano Mater.* **1**(7), 3355 (2018).

⁵⁰A. Jain, S. P. Ong, G. Hautier, W. Chen, W. D. Richards, S. Dacek, S. Cholia, D. Gunter, D. Skinner, G. Ceder, and K. A. Persson, “Commentary: The materials project: A materials genome approach to accelerating materials innovation,” *APL Mater.* **1**(1), 011002 (2013).

⁵¹M. De Jong, W. Chen, T. Angsten, A. Jain, R. Notestine, A. Gamst, M. Sluiter, C. Krishna Ande, S. Van Der Zwaag, J. J. Plata, C. Toher, S. Curtarolo, G. Ceder, K. A. Persson, and M. Asta, “Charting the complete elastic properties of inorganic crystalline compounds,” *Sci. Data* **2**(1), 150009 (2015).

⁵²F. Pedregosa, G. Varoquaux, A. Gramfort, V. Michel, B. Thirion, O. Grisel, M. Blondel, P. Prettenhofer, R. Weiss, V. Dubourg, J. Vanderplas, A. Passos,

D. Cournapeau, M. Brucher, M. Perrot, and É. Duchesnay, “Scikit-learn: Machine learning in python,” *J. Mach. Learn. Res.* **12**, 2825 (2011).

⁵³X. Tian and M. Chen, “Descriptor selection for predicting interfacial thermal resistance by machine learning methods,” *Sci. Rep.* **11**, 739 (2021).

⁵⁴L. Breiman, “Random forests,” *Mach. Learn.* **45**(1), 5 (2001).

⁵⁵S. A. Tawfik, O. Isayev, M. J. S. Spencer, and D. A. Winkler, “Predicting thermal properties of crystals using machine learning,” *Adv. Theory Simul.* **3**(2), 1900208 (2020).

⁵⁶C. Loftis, K. Yuan, Y. Zhao, M. Hu, and J. Hu, “Lattice thermal conductivity prediction using symbolic regression and machine learning,” *J. Phys. Chem. A* **125**(1), 435 (2021).

⁵⁷Z. Pan, Y. Zhou, and L. Zhang, “Photoelectrochemical properties, machine learning, and symbolic regression for molecularly engineered halide perovskite materials in water,” *ACS Appl. Mater. Interfaces* **14**(7), 9933 (2022).

⁵⁸J. He, J. Li, C. Liu, C. Wang, Y. Zhang, C. Wen, D. Xue, J. Cao, Y. Su, L. Qiao, and Y. Bai, “Machine learning identified materials descriptors for ferroelectricity,” *Acta Mater.* **209**, 116815 (2021).

⁵⁹A. Giri and P. E. Hopkins, “A review of experimental and computational advances in thermal boundary conductance and nanoscale thermal transport across solid interfaces,” *Adv. Funct. Mater.* **30**(8), 1903857 (2020).

⁶⁰J. Zhong, Q. Xi, Z. Wang, T. Nakayama, X. Li, J. Liu, and J. Zhou, “Thermal boundary conductance across solid-solid interfaces at high temperatures: A microscopic approach,” *J. Appl. Phys.* **129**(19), 195102 (2021).

⁶¹Y. R. Koh, J. Shi, B. Wang, R. Hu, H. Ahmad, S. Kerdsonpanya, E. Milosevic, W. A. Doolittle, D. Gall, Z. Tian, S. Graham, and P. E. Hopkins, “Thermal boundary conductance across epitaxial metal/sapphire interfaces,” *Phys. Rev. B* **102**(20), 205304 (2020).

⁶²R. J. Stevens, A. N. Smith, and P. M. Norris, “Measurement of thermal boundary conductance of a series of metal-dielectric interfaces by the transient thermoreflectance technique,” *J. Heat Transfer* **127**(3), 315 (2005).

⁶³J. C. Duda, C. J. Kimmer, W. A. Soffa, X. W. Zhou, R. E. Jones, and P. E. Hopkins, “Influence of crystallographic orientation and anisotropy on Kapitza conductance via classical molecular dynamics simulations,” *J. Appl. Phys.* **112**(9), 093515 (2012).

⁶⁴Z. Wei, Z. Yang, M. Liu, H. Wu, Y. Chen, and F. Yang, “Thermal boundary conductance between high thermal conductivity boron arsenide and silicon,” *J. Appl. Phys.* **127**(5), 055105 (2020).

28 June 2025 08:06:18